Open access • Journal Article • DOI:10.1109/TMECH.2010.2040900

Robotic Micromanipulation and Microassembly Using Monoview and Multiscale Visual Servoing — Source link

Brahim Tamadazte, Nadine Piat, Sounkalo Dembélé

Institutions: University of Franche-Comté

Published on: 17 Jan 2011 - IEEE-ASME Transactions on Mechatronics (IEEE)

Topics: Visual servoing and Zoom

Robotic Micromanipulation and Microassembly using Mono-view and Multi-scale visual servoing.

Brahim Tamadazte, Nadine Le Fort-Piat, Soukalo Dembélé

Robotic Micromanipulation and Microassembly using Mono-view and Multi-scale Visual Servoing

B. Tamadazte, *Member, IEEE,* N. Le-Fort Piat, and S. Dembélé,

***Abstract*—This paper investigates sequential robotic micromanipulation and microassembly in order to build 3-D microsystems and devices. A mono-view and multiple scale 2-D visual control scheme is implemented for that purpose. The imaging system used is a photon video microscope endowed with an active zoom enabling to work at multiple scales. It is modelled by a non-linear projective method where the relation between the focal length and the zoom factor is explicitly established. A distributed robotic system (xyθ system, ϕz system) with a two-fingers gripping system is used in conjunction with the imaging system. The results of experiments demonstrate the relevance of the proposed approaches. The tasks were performed with the following accuracy: 1.4 μm for the positioning error, and 0.5 $^\circ$ for the orientation error.**

***Index Terms*—Microassembly, micromanipulation, microrobotic, multiple scale visual servoing, depth-from-focus.**

I. Introduction

THE development of micro electromechanical systems (MEMS) as well as micro opto electromechanical systems (MOEMS) has led to smaller components and increasingly complex microstructures, thus requiring sophisticated micromanipulation techniques. Furthermore, no commercial success of these products is possible without reliable and cost-effective assembly and packaging technologies. Therefore, researches conducted in the last decade have led to the definition of micromanipulation and microassembly techniques [1] and the development of microrobotic cells in order to assist the human operator for the handling or the assembly of such microparts, e.g. [2], [3]. In contrast to self-assembly [4], robotic microassembly is direct, deterministic and based on serial [5] or parallel [6] approaches. Recently, the automation of microassembly tasks represents some of the ultimate goals. Meanwhile, the availability of high resolution cameras and powerful microprocessors have allowed vision systems to play a key role in the automatic assembly domain of microsystems. Therefore, vision sensors are essential to perform microhandling tasks, as well as in tele-operated, semi-automatic than full-automatic modes. Several vision techniques have been successfully implemented in the microdomain [7], [8], [9], [6], [10], [11]. Also, in the literature, it was shown that vision feedback control is an appropriate solution in the automation of microhandling and microassembly tasks. However, a large part of the control laws presented in the literature are of image-based visual servoing type; few works deal with the use of pose-based visual control techniques and still less concern multiple scale control laws approaches. In [8] and [12], the authors proposed the use of a distributed imaging system: a high resolution optical microscope delivering a local view and a camera equipped with standard lens delivering a global view of the workscene. That dual system was, then, used to realize a multi view and multi scale image-based visual servo. However, multiple scale approaches can be computed and implemented using a single imaging system. This one have to be equipped with an electronically controllable zoom (active zoom). An illustration is stated in [13], where a multiple scale image visual control using active zooming prevents the target to go out of the field of view.

In this paper, a full automatic micromanipulation and microassembly have been investigated. Our contribution concerns the design of a new visual feedback method. This method is based on a mono-view and multiple scale image-based visual servo using dynamic zoom and focus and is decomposed in two mains parts. The first part is the definition of a multiscale model of the video microscope that the parameters are obtained by applying a new calibration method. The originality of this method lies especially in the computation of the multiple scale (for each magnification step) model of the optical microscope using a 2D virtual template. Thus, the relation between the focal length and the zoom factor is established and introduced in the visual control law. The second part concerns the development of the visual-based control law using only a single view. Due to the weak depth of field of the video microscope, a depth-from-focus method is used to compute the depth information between the microscope and the gripper. This information is used in the visual control law in order to maintain the focusing of the video microscope on the micromanipulator during the micromanipulation or microassembly process.

This new approach is well appropriated for the performing of micromanipulation and microassembly processes needed a very high precision. The method and algorithms proposed had been implemented on an experimental setup including a five degrees of freedom (dof) distributed robotic system (three dof ($xy\theta$) dedicated to the mobile platform and two dof ($z\phi$) dedicated to the manipulator), a gripping system, an imaging system and a clean environment. The micro-objects to handle

The authors work at the FEMTO-ST Institute, UMR CNRS 6174-UFC/ENSMM/UTBM. Automatic Control and Micro-Mechatronic Systems Department (AS2M). 24 rue Alain Savary, 25000 Besançon, France. Corresponding e-mail : brahim.tamadazte@ens2m.fr. Phone: +33 (0)3 81 40 27 99, Fax: (33) 03 81 40 28 09, http://www.femto-st.fr.

This work is partially conducted with financial support from the project "Hybrid Ultra Precision Manufacturing Process Based on Positional and Self assembly for Complex Micro-Products (HYDROMEL NMP2-CT-2006-026622)" funded by the European Commission.

Manuscript received .

or assemble consist of 400 μm $\times$ 400 μm $\times$ 100 μm silicon components.

This paper is structured as followed: Section II presents the decomposition of the robotic micromanipulation process as a sequence of basic tasks. Section III develops the concepts of the mono view multiple scale visual control. A multiple scale modelling of the photon video microscope is proposed in section IV. The corresponding calibration approach combining robotic and vision is also presented. Section V exposes the vision algorithms used in the experiments. They include the tracking of the micro-object and of the gripper in the images of the scene, the autofocus achievement and the recovery of depth. The experimental setup and related results are presented in section VI. They show the relevance of the proposed concepts.

II. Task planning of robotic micromanipulation

Robotic manipulation corresponds to the handling and positioning of microparts by means of a robotic system in conjunction with a gripping system and an imaging system.

Let the purpose of the primary (manipulation) task be a cyclical pick up of microparts from the initial locations and their place in target locations. The function chart of Fig. 1 is the representation of a sequence enabling the achievement of the pick-and-place process. Some tasks require high accuracy, so it is recommended to check up on their success rate. The chart representing the sequence can include this possibility as illustrated in Fig. 1.

- task 1: autofocusing. This task enables to keep the micro-object focused in the images of the scene during the process.
- task 2: detection of the component. The gripping of the part assumes its recognition and localization in the scene.
- task 3: aligning of the component in parallel to the axis. This task includes the increasing of the scale.
- task 4: positioning and centering of the component under the gripper. This task includes the increasing of the scale.
- task 5: opening of the gripper fingers.
- task 6: descent of the gripper.
- task 7: closing of the gripper fingers. Every finger-tip (p_1 and p_2 for the upper and lower tip, respectively) is displaced into a contact point (p_1^* and p_2^*, respectively) located in the gripping plane of the micropart.
- task 8: grasping of the component. This task is performed using a vision-based control law.
- task 8: ascent of the gripper with the component.
- task 9: positioning of the component in the target place.
- task 10: descent of the gripper with the component.
- task 11: opening of the gripper in order to release the component. This task is decisive in the process, because of the high level of capillary forces [14]. The micro-object tends to stick on the fingers after their opening.
- task 12: positioning of the gripper back to its initial place.

The sequence of tasks can be considered as a model for the behavior of the systems dedicated to perform the manipulation task. Consequently, it can be used as means to perform the control of these systems. The manipulation appears as a sequence of servo controls including visual controls. As the optical microscope used is a multiple scale imaging systems (equipped with a dynamic zooming system), dynamic and multiscale visual servoings are developed here.

III. Multiple scale visual control

Image-based visual control, more particularly 2-D visual servoing is accurate and robust towards the errors of modelling of the imaging and the robotic systems [15]. Thus, this kind of servoing is suitable for the achievement of basic manipulation tasks. Among the various choices of control laws, exponential and polynomial decrease of error exhibit high efficiency.

A. Modelling of image-based visual control law integrating the zoom control

From a general point of view, the aim of vision-based control schemes is to minimize the error $\mathbf{e}(t)$ [16] typically defined by:

$$\mathbf{e}(t) = \mathbf{s}(\mathbf{m}(t)) - \mathbf{s}^* \tag{1}$$

where $\mathbf{m}$ is a set of visual information $\mathbf{s}$ extracted from the image (e.g. the image coordinates of interest points) and $\mathbf{s}^*$ the desired visual features. In our case, the vector $\mathbf{e}$ contains the coordinates of the four corners of the bonding box (tracking windows) delimiting the micro-object to be handling. The introduction of the zoom control in the final visual control law can be summarized by adding a new degree of freedom. In multiple scale visual control laws, the focal length f, the desired value of the visual feature points $\mathbf{s}^*$ and the current value of these points $\mathbf{s}$ are functions of the zoom factor ζ: $f(\zeta)$, $\mathbf{s}^*(\zeta)$ and $\mathbf{s}(\zeta)$, (Fig. 2). Therefore, (1) becomes:

$$\mathbf{e}(t) = \mathbf{s}(\mathbf{m}(\mathbf{t}, \zeta)) - \mathbf{s}^*(\zeta) \tag{2}$$

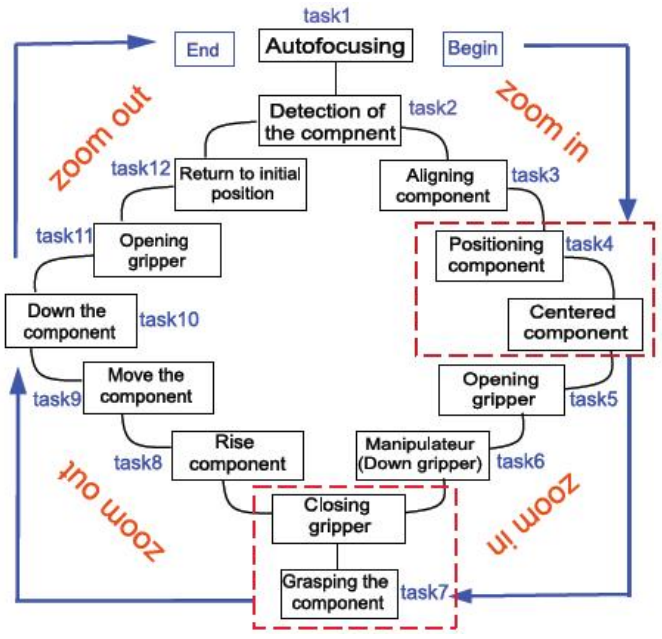

Fig. 1. Sequential function chart of the picking and placing of a microcomponent.

Designing the control scheme requires the computation of the relationship between the time variation of $\mathbf{s}(\zeta)$ and the camera velocity. Let the spatial velocity of the camera (optical microscope) be denoted by $\mathbf{v} = (v, \omega)$: $\mathbf{v}$ is the instantaneous linear velocity and ω is the instantaneous angular velocity. In the case of controlling a 6 dof robot, $v = (v_x, v_y, v_z)^\top$ and $\omega = (\omega_x, \omega_y, \omega_z)^\top$. In our case, a 5 dof microrobot is considered e.g., 3 dof (x, y, θ) for the positioning platform and 2 dof (z, ϕ) for the micromanipulator, so $\mathbf{v} = (v_x, v_y, v_z)^\top$ and $\omega = (\omega_\theta, \omega_\phi)^\top$. In [15], the relationship between the velocity variations of $\dot{\mathbf{s}}$ and $\mathbf{v}$ is given by:

$$\dot{\mathbf{s}} = \mathbf{L_s}\mathbf{v} \tag{3}$$

where $\mathbf{L_s}$ ($\mathbf{L_s} \in \mathbf{R}^{n\times 6}$) is the interaction matrix (also called jacobian image) related to $\mathbf{s}$. The parameter n represents the number of visual features used.

In our case, $\mathbf{L_s}$ is function of $\mathbf{s}$, ζ and Z^*, so the (3) becomes:

$$\dot{\mathbf{s}} = \mathbf{L_s}(\mathbf{s}, Z^*, \zeta)\mathbf{v} \tag{4}$$

where Z^* is the desired depth information processed by the depth-from-focus method presented in the section V-B. If we consider a 3-D point $\mathbf{P}$ with the coordinates (X, Y, Z) in the camera frame $\mathcal{R}_c$, which can be projected in the image frame $\mathcal{R}_I$ with the coordinates $p = (x, y)$, we obtain:

$$x = X/Z = (u - x_0)/f(\zeta) \tag{5}$$

$$y = Y/Z = (u - y_0)/f(\zeta) \tag{6}$$

where (x_0, y_0) and $f(\zeta)$ are the optical microscope intrinsic parameters (these parameters are computed using the calibration method presented in the section IV). More precisely, (x_0, y_0) are the coordinates of the principal point and (u, v) are the coordinates of the image point p expressed in pixel units.

Performing time derivation of (5) and (6), with some handling (more details can be found in [15]) we obtain:

$$\mathbf{L_s} = \begin{pmatrix} \mathbf{L_s}(x(n), Z^*, \zeta) \\ \mathbf{L_s}(y(n), Z^*, \zeta) \end{pmatrix} \tag{7}$$

where:

$$\mathbf{L_s}(x(n), Z^*, \zeta) = \begin{pmatrix} \frac{-1}{Z^*} & 0 & \frac{x_1(\zeta)}{Z^*} & x_1(\zeta)y_1(\zeta) & -1 - x_1^2(\zeta) & y_1(\zeta) \\ \frac{-1}{Z^*} & 0 & \frac{x_2(\zeta)}{Z^*} & x_2(\zeta)y_2(\zeta) & -1 - x_2^2(\zeta) & y_2(\zeta) \\ \frac{-1}{Z^*} & 0 & \frac{x_3(\zeta)}{Z^*} & x_2(\zeta)y_2(\zeta) & -1 - x_3^2(\zeta) & y_3(\zeta) \\ \frac{-1}{Z^*} & 0 & \frac{x_4(\zeta)}{Z^*} & x_2(\zeta)y_2(\zeta) & -1 - x_4(\zeta)^2 & y_4(\zeta) \end{pmatrix} \tag{8}$$

$$\mathbf{L_s}(y(n), Z^*, \zeta) = \begin{pmatrix} 0 & \frac{-1}{Z^*} & \frac{y_1(\zeta)}{Z^*} & 1 + y_1^2(\zeta) & -x_1(\zeta)y_1(\zeta) & -x_1(\zeta) \\ 0 & \frac{-1}{Z^*} & \frac{y_2(\zeta)}{Z^*} & 1 + y_2^2(\zeta) & -x_2(\zeta)y_2(\zeta) & -x_2(\zeta) \\ 0 & \frac{-1}{Z^*} & \frac{y_3(\zeta)}{Z^*} & 1 + y_3^2(\zeta) & -x_3(\zeta)y_3(\zeta) & -x_3(\zeta) \\ 0 & \frac{-1}{Z^*} & \frac{y_4(\zeta)}{Z^*} & 1 + y_4^2(\zeta) & -x_4(\zeta)y_4(\zeta) & -x_4(\zeta) \end{pmatrix} \tag{9}$$

We can define the relationship between the camera velocity and the time variation of $\mathbf{e}$ given by (1). This relation is:

$$\dot{\mathbf{e}} = \mathbf{L_s}\mathbf{v} \tag{10}$$

If we want to ensure an exponential decoupled decrease of the error $\mathbf{e}$, we can write:

$$\dot{\mathbf{e}} = \lambda\mathbf{e} \tag{11}$$

where λ is a positive gain.

Therefore, from (10) and (11), the control law can be deduced.

$$\mathbf{v} = -\lambda\mathbf{L_s^+}\mathbf{e} \tag{12}$$

with $\mathbf{L_s^+}$ is the pseudo-inverse of $\mathbf{L_s}$. If $det(\mathbf{L_s}) \neq 0$ it is possible to use directly the inverse $\mathbf{L_s^{-1}}$ of the interaction matrix $\mathbf{L_s}$, giving the control law:

$$\mathbf{v} = -\lambda\mathbf{L_s^{-1}}\mathbf{e} \tag{13}$$

To improve the convergence rate and the stability of the developed control law, we have implemented an adaptive gain (the gain decreases when the error decreases). Therefore, the positive gain λ is replaced by the adaptive gain λ_a processed as follows:

$$\lambda_a = (\lambda_{min} - \lambda_{max})exp^{-\rho\|\mathbf{e}\|} + \lambda_{max} \tag{14}$$

where $\lambda_{\max}$ and $\lambda_{\min}$ are the maximum and minimum values of λ_a. The experimental results presented in this paper are obtained with $\lambda_{\min}$ = 0.1 and $\lambda_{\max}$ = 1. The parameter ρ allows the tuning of the exponential decreasing rate of the error and $\| \mathbf{e} \|$ is its related norm. The evolution of the λ_a during a micromanipulation task is shown in Fig. 10.

The multiple scale visual servoing scheme can be represented by the function chart given in Fig. 2.

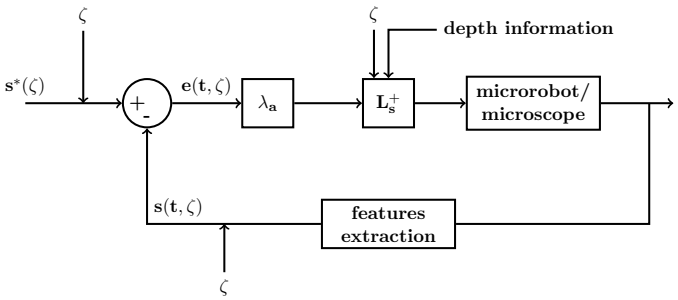

Fig. 2. Multiple scale image-based visual servoing scheme.

B. Gripper closing controlled by visual servoing

Once the micro-object and the gripping end-effectors are positioned to their respective desired positions, it is necessary to control the gripping system in the aim to grip the micro-object (gripping task). An appropriate tightening force is required, which would enable the gripping without destruction of one or both the micro-object and the gripper tips. In this case, a control approach based on microforce feedback control law is used. Our gripping system is not equipped with a microforce sensor, so the gripping task is ensured by a vision-based control technique. This control law consists of regulating towards zero the distance between the desired value $\mathbf{s}_f^*$ and the current value $\mathbf{s}_f$ of the image points.

Let the distance corresponding to the task function be $\mathbf{e}_1(t)$:

$$\mathbf{e}_1(t) = \Delta(\mathbf{s}_f^* - \mathbf{s}_f(t)) \tag{15}$$

The polynomial decrease of the error $\mathbf{e}_1(t)$ leads to the following control:

$$v_{d1}(t) = \frac{\mathbf{e}_1(t)}{N} \tag{16}$$

where $v_{d1}(t)$ is the input for the actuator of the first fingertip of the gripper and N is a constant integer. For the second finger tip, the input $v_{d2}(t)$ is deduced by symmetry and it is given by:

$$v_{d2}(t) = -v_{d1}(t) = \frac{\mathbf{e}_1(t)}{N} \tag{17}$$

IV. Multiscale modelling of the photon video microscope

A. Basic model

The standard lens based image source is modelled by the non linear projective model. The latter includes: the intrinsic parameters inherent to the imaging system (i.e. the focal length f, the scale factors k_x, k_y in x and y directions), the principal point coordinates (x_o, y_o), the extrinsic parameters corresponding to the position and orientation of the focusing element frame (usually called camera) with respect to the scene frame i.e. the translation components $\mathbf{T_x}$, $\mathbf{T_y}$, and $\mathbf{T_z}$, and for example, Euler angles α, β and γ, and the distortion parameters: the radial $(r_1, r_2, ...)$ and tangential $(t_1, t_2, ...)$ distortion coefficients.

The improvement of technology enables the manufacturing of isotropic image sensors in which the scale factors along x and y are identical:

$$k_x = k_y = k \tag{18}$$

The microscope-based image source is an optical imaging and thus can be modelled by the non linear projective model. However, the quality of a laboratory microscope is usually better than that of a standard lens, so experimental values of distortion parameters are very weak. They range from 10^{-8} μm^{-2} to 10^{-10} μm^{-2} [17], [18]. As a consequence the distortion can be neglected and so the video microscope can be modelled by the linear projective model. This model consists of a perspective projection of a scene point $\mathbf{P}$ onto a pixel p in the retinal plane through the optical center.

Let $\mathbf{P}$ and p be represented by the homogeneous vector $(\mathbf{X}, \mathbf{Y}, \mathbf{Z}, \mathbf{1})^\top$ and $(x, y, w)^\top$, respectively. The model can be written:

$$p = \mathbf{QP} \tag{19}$$

where $\mathbf{Q}$ is the 3×4 homogeneous projection matrix of the image source. It is written:

$$\mathbf{Q} = \mathbf{K} \begin{pmatrix} 1 & 0 & 0 & 0 \\ 0 & 1 & 0 & 0 \\ 0 & 0 & 1 & 0 \end{pmatrix} \mathbf{D} \tag{20}$$

The general form of the matrix $\mathbf{K}$ is given by:

$$\mathbf{K} = \begin{pmatrix} k_x f & -k_x f \cos(\psi) & x_o \\ 0 & k_y f / \sin(\psi) & y_o \\ 0 & 0 & 1 \end{pmatrix} \tag{21}$$

where ψ is the angle between the image axes u and v. In general, the pixels are square, so $\psi = 90\ ^\circ$.

Taking into account all the simplifications presented above, the matrix $\mathbf{K}$ becomes:

$$\mathbf{K} = \begin{pmatrix} kf & 0 & x_o \\ 0 & kf & y_o \\ 0 & 0 & 1 \end{pmatrix} \tag{22}$$

Concerning the matrix $\mathbf{D}$, it combines the rotation matrix $\mathbf{R}$ and the translation vector $\mathbf{T}$ as follows:

$$\mathbf{D} = \begin{pmatrix} \mathbf{R}_{3\times3} & \mathbf{T}_{1\times3} \\ 0 & 1 \end{pmatrix} \tag{23}$$

The rotation matrix which gathers the three rotation angles (if the Euler angles α, β, and γ are considered) is given by:

$$\mathbf{R} = \mathbf{R_x}\ \mathbf{R_y}\ \mathbf{R_z} \tag{24}$$

where:

$$\mathbf{R_x} = \begin{pmatrix} 1 & 0 & 0 \\ 0 & \cos\alpha & -\sin\alpha \\ 0 & \sin\alpha & \cos\alpha \end{pmatrix} \tag{25}$$

$$\mathbf{R_y} = \begin{pmatrix} \cos\beta & 0 & \sin\beta \\ 0 & 1 & 0 \\ -\sin\beta & 0 & \cos\beta \end{pmatrix} \tag{26}$$

$$\mathbf{R_z} = \begin{pmatrix} \cos\gamma & -\sin\gamma & 0 \\ \sin\gamma & \cos\gamma & 0 \\ 0 & 0 & 1 \end{pmatrix} \tag{27}$$

B. Multiscale model

Multiscale calibration is required because the video microscope works at multiple zoom or magnification. Thus, it is necessary to introduce the zoom factor ζ in the previous intrinsic model:

$$\mathbf{K}(\zeta) = \begin{pmatrix} f(\zeta)k & 0 & x_o \\ 0 & f(\zeta)k & y_o \\ 0 & 0 & 1 \end{pmatrix} \tag{28}$$

It can be noticed that the principal point (center of the zooming) coordinates (x_0, y_0) do not change during the decreasing and the increasing of magnification (see, Fig. **??**). The coordinates of the principal point are computed by tracking the displacements of a micro-object placed on the positioning platform. The displacements of the micro-object are directly linked to the magnification changes.

In a microscope where a tube is associated with the lens, the parameter f in the previous equations becomes the sum of the objective focal length f_{ob} and the length of this tube l_t [17]:

$$f = f_{ob} + l_t \tag{29}$$

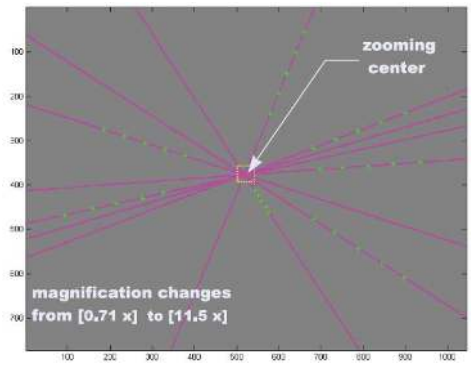

Fig. 3. Center of zooming.

The relationship that links f with ζ is given by:

$$\zeta = \frac{l_t}{f_{ob}} \tag{30}$$

Knowing l_t, it is possible to compute the objective focal length f_{ob} by:

$$f_{ob} = \frac{l_t}{\zeta} \tag{31}$$

From (29) and (30), a relationship can be established between f and ζ. This relationship is given by:

$$\zeta = \frac{l_t}{f - l_t} \tag{32}$$

then,

$$f = \left(1 + \frac{1}{\zeta}\right) \tag{33}$$

It is also possible to generalize the expression of f according to the variation of ζ. Therefore, a non linear relation links the zoom factor ζ with the focal length f is established. This relation can be represented by a polynomial relation as follows:

$$f = \frac{l_t + l_t\ a_i\ \left(\ \zeta^{10}\quad \zeta^9\quad \cdots\quad 1\ \right)^\top}{a_i.\left(\ \zeta^{10}\quad \zeta^9\quad \cdots\quad 1\ \right)^\top} \tag{34}$$

then,

$$f = lt\left(1 + \frac{1}{a_i(\ \zeta^{10}\quad \zeta^9\quad \cdots\quad 1)^\top}\right) \tag{35}$$

where:

$$a_i = [a_1\ a_2 \cdots a_{11}] \tag{36}$$

is (1×11) vector whose elements are polynomial coefficients.

C. Computing the parameters at multiple scale

There are similarities between vision sensing at the macro, meso and microscales. For each scale a 2-D image is formed from a 3-D object through an optical lens system. As they are modelled by the same method, the same approaches of calibration can be achieved. These techniques are roughly classified into two families: photogrammetric calibration approaches and self calibration approaches. In the first method, the model parameters are computed by observing a calibration object (3-D pattern) whose geometry is known with high accuracy. The calibration object usually consists of 2 or 3 planes, ones orthogonal to each other. An unique plane object is also used, but in this case, several images at different 3-D orientations are considered [19], [20]. In the second method, it is not necessary to use a calibration pattern. The correspondences between images of a static scene are enough to recover both intrinsic and extrinsic parameters. In this case the accuracy is not as good as in the previous approaches [20].

In any case, an important number of correspondences $p - \mathbf{P}$ are required. Calibration is performed in two stages. The first stage consists of roughly estimating the projection matrix $\mathbf{Q}$ by resolving the DLT (Direct Linear Transformation) which is obtained by combining the projection equations for points of correspondence. The second stage enables the fine estimation of the parameters by minimizing a criterion, usually the geometric error δ.

$$\delta = \sum_i d(p_i, \mathbf{Q}\mathbf{P}_i) \tag{37}$$

Even if the same algorithm can be implemented both in macro and microscales, there are some fundamental differences between a standard lens and a high magnification lens. A microscope is characterized by weaker DOF (Depth-Of-Field) and FOV (Field-Of-View).

As a consequence of these limitations, a 3-D calibration template cannot be used. The pattern is reduced to a planar object that should be almost parallel to the lens. A video microscope is heavy and cumbersome and is thus not easy to manipulate. These constraints complicate the calibration of the video microscope. On the other hand, the presence of accurate motion sources like xyz stages enables accurate motions of the calibration sample plane and facilitates the calibration.

Instead of using a real pattern or virtual points, the proposition is to use the power of image processing: the center of gravity of a micrometric part is tracked in the images of the scene. The micropart is moved accurately (with steps of 300 μm) by a xyz stage, so its central position in the scene is known with high accuracy using an autocorrelation detection method. These positions are used to synthesize a virtual image which is used in the algorithm presented previously. This approach enables high accuracy in computing of the model parameters. The approach is also simple, as it does not require the micromachining of any particular pattern. The components necessary for the assembly are directly used.

V. Vision algorithms

A. Tracking of micro-objects and end-effectors

Image processing and vision are very important in visual servoing. The following conditions are essential for the success of the control:

- Vision should be able to deliver visual information at a rate close to the sampling frequency of the robot control;
- Interaction matrix should be explicitly calculated;
- Control must be robust to little occlusions (like the passage of the micro-object under the gripper).

There are several methods of visual tracking which are usually classified into two groups. The first group consists of the tracking of local features like lines, segments, points, edges, etc. [21]. The results of these techniques highly depend on the quality of the images and remain very sensitive to feature detection [22]. The other group contains methods that perform a comparison between two frames in the image sequence by minimizing an error based on the image brightness. These methods take into account some parameters like motion, deformation or illumination parameters between the two frames or the frame and a template.

Images of the planar silicon microparts as well as those of the gripper tips are not very sharp because of the properties of the microscope. Consequently, a robust tracking algorithm able to work in real-time is required. The tracking is achieved by an algorithm proposed in [22] and [23]. This algorithm is based on the second-order-minimization. It has a far superior convergence rate than other techniques, which is an important property for real-time tracking. For instance, if we consider the window I^* of m pixels which contains the micro-object as the reference, then tracking I^* in the global current image I consists in computing a vector V. This vector of (8×1) size includes the parameters of the projective transformation H. It transforms each pixel p^* from the reference image I^* to the current image I using the following relationship:

$$I\left(w(H)(p_i^*)\right) = I^*(p_i^*) \tag{38}$$

In the reference [24], for an approximation $\hat{V}$ of V, or $\hat{H}$ of H, the problem is to find an incremental transformation $H(V)$ such as the difference between the region image I transformed with the composition $w(\hat{H}) \circ w\big(H(V)\big)$, and the corresponding region in the image I^* is zero. It involves to find the vector V such that $\forall i \in (1, 2, ..., q)$, we have:

$$y_i(V) = I\left(w(\hat{H}) \circ w\left(H(V)\right)(p_i^*)\right) - I^*(p_i^*) = 0 \tag{39}$$

where $w(H)$ represents an automorphism transformation.

Let be the (q $\times$ 1) vector $y(V)$ which represents these differences between I and I^*. Therefore, we can write:

$$y_i(V) = [\ y_1(V),\ y_1(V),\ \cdots\ y_q(V)\ ]^\top \tag{40}$$

The solution of the equation (40) can be computed by finding $V = \tilde{V}$ which verifies the following system:

$$y(\tilde{V}) = 0 \tag{41}$$

In our case, for the micro-object, the coordinates of the four points delimiting the bounding box (searching template W_1) of the micropart is estimated (Fig. 4). For the above finger the coordinates of the tip (point $p_1 = (u_1, v_1)$) is estimated. This point is the bottom left point of the searching template W_2 delimiting the gripper tip. The coordinates of the below tip (point $p_2 = (u_2, v_2)$) is deduced by symmetry.

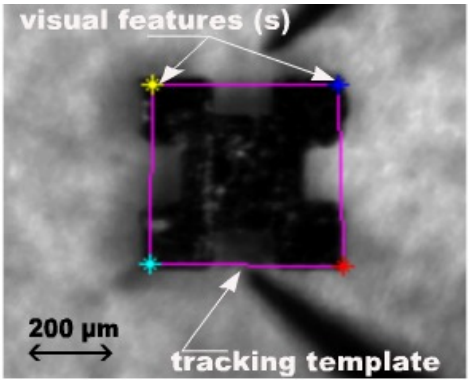

Fig. 4. Image captured during the micro-object tracking.

B. Autofocus achievement and depth recovery

Because of the weakness of the DOF, an autofocus method is implemented in order to guarantee focused images during the experiments. The depth of the scene is scanned step by step, images are acquired and the focus is estimated. The system is repositioned at the position where the focus estimation is the highest. Three focus estimators (presented in [25]) have been tested: the variance, the intercorrelation and the Brenner gradient. The variance focus estimator given by (42), is selected as it makes a trade off between resolution and computing time.

$$F_{\mathrm{Var}} = \frac{1}{H.W.\mu} \sum_H \sum_W (i(x,y) - \mu)^2 \tag{42}$$

where H and W are the image height and width, i is the (x, y) pixel intensity and μ is the mean of image intensity, respectively.

The representation of the focus estimation according to z motion gives two peaks (Fig. 5). The low peak corresponds to the gripper and the high peak corresponds to the platform and the component. Therefore, it is possible to determine the depth Z^* between the camera and the micro-object:

$$Z^* = Z_o - Z_g \tag{43}$$

where Z_o is the distance between the micro-object and the gripper and Z_g represents the distance between the camera (microscope) and the gripper.

This depth information Z^* is used to servo the motion of the video microscope on the motion of the gripper, see Fig. 6.

VI. Experimental setup

A. Micromanipulation and microassembly workcell

The above concepts were validated using the microassembly workcell shown in Fig. 7.(a). The complete workstation

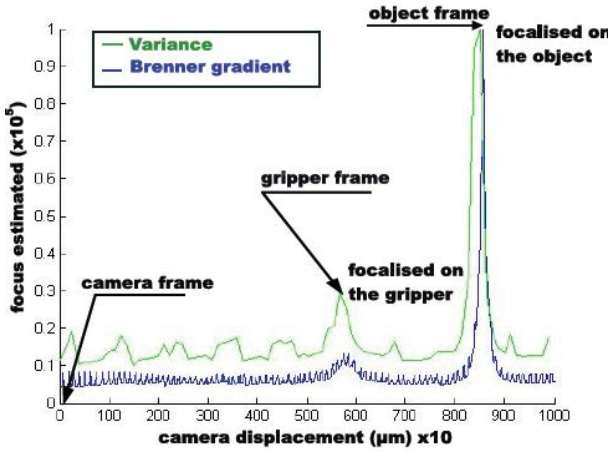

Fig. 5. Focus estimation result.

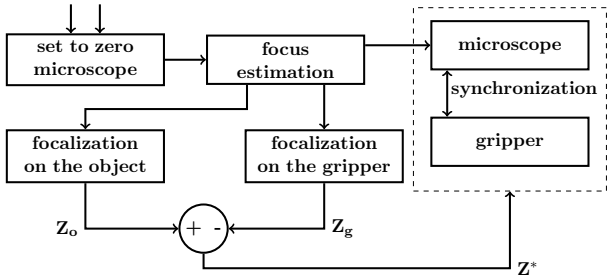

Fig. 6. Focus-based gripper tracking

includes a robotic system in combination with a gripping and an imaging system. The whole setup is located inside a controlled environment and posed on a vibration-free table. Two PCs connected by an Ethernet link process the information, the first (Pentium (R) D, CPU 2.80 G Hz, 2 Go of RAM) is dedicated to vision algorithms while the second (Pentium (R) 4, CPU 3.00 G Hz, and 1 Go of RAM) is used for control algorithms. In a kinematic point of view, the workstation is a five dof robotic system. Three dof (x, y and z) in translation are achieved by three high accuracy linear stages and two dof (θ and ϕ) in rotation are achieved by two high accuracy angular stages (all from Polytec PI). The translation motions x,y, and z are characterized by a resolution $r = 0.007$ μm, an increment $i = 0.05$ μm, a velocity $v_t = 1.5$ mm/s, a stroke of $s_t = 25$ mm. The specifications of the angular motions are: $r = 26$ μrad, $i = 26$ μrad and speed $v_r = 45$ deg/s. These dof are distributed into two robotic systems: a $xy\theta$ system and a $z\phi$ system. The former system (the positioning platform) is equipped with a compliant table (the table is supported by three springs) and enables the positioning in the horizontal plane. The latter system (the manipulator) supports the gripper and enables the vertical positioning and spatial orientation of micro-objects.

A Microrobotic Microprehensile On Chip (MMOC) gripper (Fig. 8) developed in the department AS2M of FEMTO-ST Institute is used for the handling of micro-objects [26]. It is a two-fingers gripping system with four dof (two dof by finger).

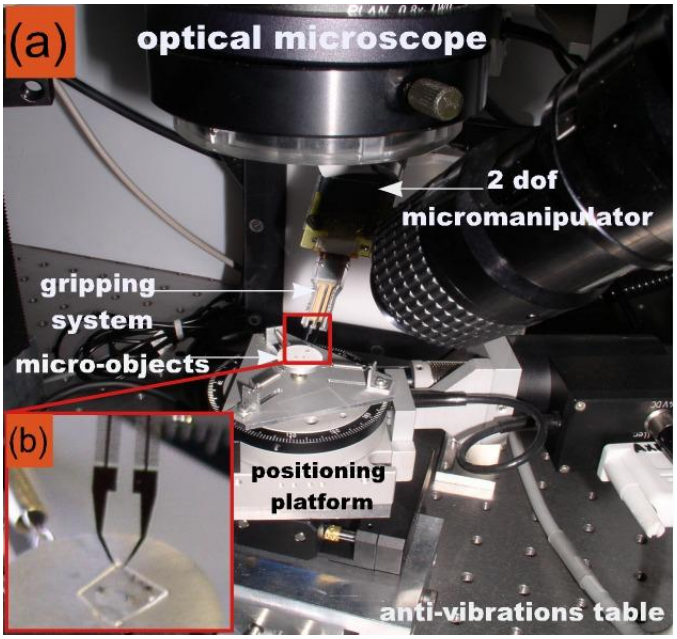

Fig. 7. Microassembly workcell. Image (a) illustrates a global view of station and image (b) shows a zooming view in the MMOC.

It enables open-and-close motions as well as up-and-down motions. Every finger is a piezoelectric bimorph with two end-effectors made of silicon layers (12 μm and 400 μm) separated by an oxide layer (1 μm) (Fig. 8). Modularity was an important design criterion during development, and the MMOC microgripper has been designed in order to use different end-effectors, e.g. silicon finger tips, nickel finger tips. It can grab a high variety of objects according to the type of material and the end-effectors shape: planar silicon micro-objects, balls, gears, optical fibers etc.

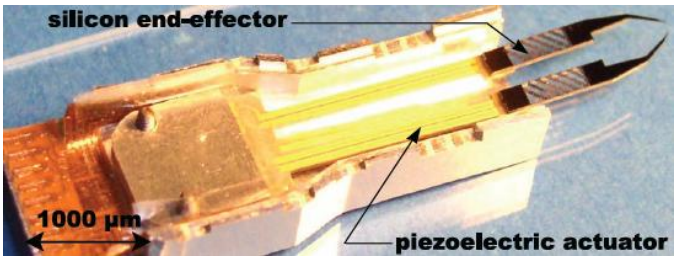

Fig. 8. Photography of the MMOC gripping system.

The imaging system is a video stereo microscope of the type LEICA MZ 16 A. It delivers a top view of the work scene. The zoom (and thus the magnification) and the focus are motorized and controlled by a PC. The FOV varies from 700 μm $\times$ 900 μm (with a resolution of 1.4 μm) at the maximum magnification to 20 mm $\times$ 25 mm (with a resolution of 21 μm) at the minimum magnification. The DOF varies from 2.9 mm to 0.035 mm and the work distance is approximately 130 mm. The workcell is also equipped with a long tube video microscope for the side view but this latter is not considered in this paper.

The objects to manipulate are structures etched in a silicon wafer of different sizes (see Fig. **??**). They have at least a notch of 100 μm on each side enabling them to be assembled to each other to form 3-D structures.

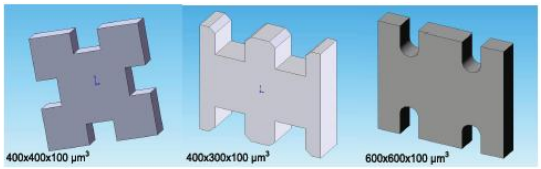

Fig. 9. Silicon microcomponents of experiments.

B. Optical microscope calibration results

The optical microscope calibration involves two stages: the establishment of the relation between the scale k and zoom ζ factors and the computing of the intrinsic parameters $\mathbf{K}$ at a given zoom factor ζ.

A metal object with three holes is used in this stage. The diameters of the holes are estimated to d_1 = 1961.5 μm, d_2 = 1037.5 μm and d_3 = 429.85 μm using a SEM (Scanning Electron Microscope) of r = 10 nm resolution. According to the zoom factor the relevant hole image is considered.

The zoom factor ζ (called magnification according to the supplier) is modified with a step of 0.05$\times$ and then 172 images are acquired. In every image the relevant hole is detected using the normalized correlation and the scale factor k corresponding to the ratio of the diameter (d_1, d_2 or d_3) of the hole in μm and in pixel is computed.

For the second stage of calibration, a planar virtual pattern is achieved from the tracking of a silicon micro-object of 400 μm $\times$ 400 μm $\times$ 100 μm.

Using the calibration method presented above, it is possible to compute the extrinsic parameters α, β, γ, $\mathbf{T_x}$ and $\mathbf{T_y}$ and the intrinsic parameters k_x, k_y, f and the coordinates of the principal point (x_o, y_o). It remains to define the third component of the translation vector $\mathbf{T_z}$ and the optical microscope working distance d. The $\mathbf{T_z}$ can be computed using the relationship given in [17]:

$$\mathbf{T}_z = f_{ob}\,\frac{\zeta+1}{\zeta}. \tag{44}$$

It is also possible to write the following approximation:

$$\mathbf{T}_z \approx f + d \tag{45}$$

From (45), it is possible to compute the working distance d:

$$d \approx \mathbf{T}_z - f \tag{46}$$

Now, all the calibration parameters (intrinsic and extrinsic) of the optical microscope are computed. These parameters are summarized in the Table I for the zoom factor position $\zeta = 38\times$.

TABLE I
CALIBRATION RESULTS.

intrinsic parameters		extrinsic parameters	
k_x	3.6444 μm^{-1}	α	88.73 °
k_y	3.6444 μm^{-1}	β	- 27.26 °
f	11.466 $\times$ 10^3 μm	γ	4.01 °
(x_o, y_o)	(473, 337) (pixels)	$\mathbf{T_x}$	8.82 (mm)
d	13.144 (cm)	$\mathbf{T_y}$	9.63 (mm)
M	3.8$\times$	$\mathbf{T_z}$	13.156 (cm)

C. Micromanipulation and assembly results

As presented previously, the basic tasks of aligning (task 5) and centering (task 6) are performed by visual servoing with the exponential decrease of error and adaptive gain, while the task of closing (task 9) is performed by another visual control with a polynomial decrease of error. Figure 10.(a) shows the result of the centering of the micropart with respect to the gripper (basic task 6). It can be seen that the implementation of an adaptive gain prevents the overshoot of the reference position. The final error is about 0.2 pixel (0.28 μm) in x and y directions. Figure 10.(b) shows the result of the micro-object alignment parallel to the x axis (basic task 5). It can be seen that the angle decreases exponentially to zero. The final error is about 0.5 degrees. This very small value shows the relevance of the control law.

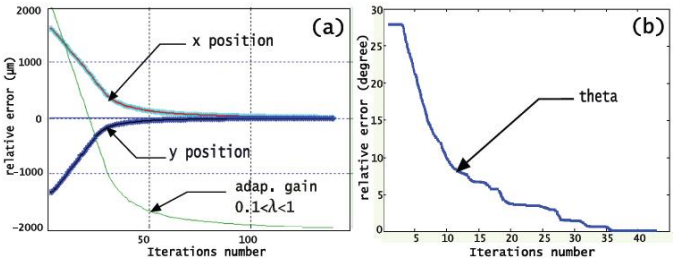

Fig. 10. Centering and orientation errors versus the number of iterations.

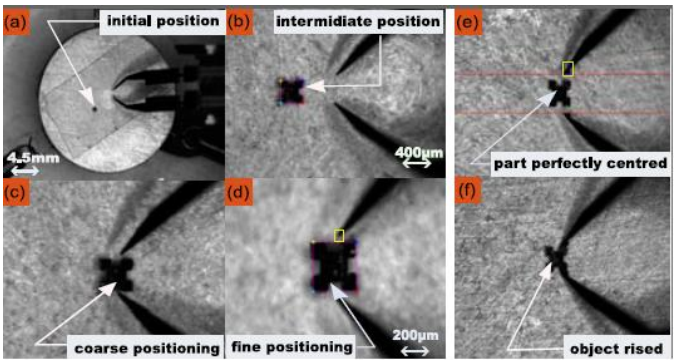

Fig. 11. Some shots during the aligning, positioning, centering, gripping and rising of the micro-object. Image (a) illustrates the initial position of the micro-object with a low magnification, images (b), (c) and (d) show intermediate positions during the control of the positioning platform.

D. Pick-and-place cycle results

The sequence of tasks represented in Fig. 1 which models the pick-and-place of a silicon micropart, is performed several

TABLE II
RESULTS CHOSEN TO REPRESENT DIFFERENT SCENARIOS ENCOUNTERED DURING THE EXPERIMENTS.

N °	task	init. pos.	prec.	note	result
	aligning (θ)	14 °	0.09 °		success
	centering (x, y)	1029 μm	0.43 μm		success
1	closing (e_1)	163 μm	1.72 μm		success
	ascent	↗	↗ [a]		success
	transfer	↗	↗		success
	release	↗	↗		success
	aligning (θ)	32 °	0.61 °		success
	centering (x, y)	1015 μm	4.91 μm		success
2	closing (e_1)	163 μm	1.77 μm	Ov. [b]	success
	ascent	↗	↗		success
	transfer	↗	↗		success
	release	↗	↗		success
	aligning (θ)	21 °	0.27 °		success
	centering (x, y)	1321.5 μm	0.77 μm	Oc. [c]	success
3	closing (e_1)	163 μm	1.44 μm		success
	ascent	↗	↗		success
	transfer	↗	↗		success
	release	↗	↗		success
	aligning (θ)	7.53 °	0.68 °		success
	centering (x, y)	992.5 μm	6.16 μm		failure
4	closing (e_1)	× [d]	×		failure
	ascent	×	×		failure
	transfer	×	×		failure
	release	×	×		failure
	aligning (θ)	33.8 °	×	Oc.	failure
	centering (x, y)	1.75 μm	×		failure
5	closing (e_1)	163 μm	×		failure
	ascent	×	×		failure
	transfer	×	×		failure
	release	×	×		failure
	aligning (θ)	13 °	0.24 °		success
	centering (x, y)	560.7 μm	0.86 μm		success
6	closing (e_1)	163 μm	×	E.F. [e]	failure
	ascent	×	×		failure
	transfer	×	×		failure
	release	×	×		failure
	aligning (θ)	15.5 °	0.52 °		success
	centering (x, y)	348.2 μm	0.64 μm		success
7	closing (e_1)	163 μm	1.11 μm		success
	ascent	↗	↗		success
	transfer	↗	↗		success
	release	×	×	C.F. [f]	failure

[a] [↗] represents the success of the task
[b] [Ov.] indicates the presence of an overshoot in the control
[c] [Oc.] represents the case when the micro-object passed under the gripper
[d] [×] represents the failure of the task
[e] [E.F.] indicates the presence of important electrostatic effects between the gripper and the micro-object
[f] [C.F.] indicates the presence of important capillary forces preventing the release of the micro-object

times (fifty cycles) in order to estimate the relevance of concepts. Initial and final positions and orientations of the micropart change from cycle to cycle in order to take into account the maximum of possible cases. Let the success rate be:

$$success\ rate = \frac{succeed\quad cycles}{total\quad cycles} \tag{47}$$

Several conclusions can be made from these experiments; the first lesson is the robustness of the visual tracking used. Despite the weak quality of the scene images and a great occlusion, the algorithm can track the micropart. It continues to work for an occlusion of 1/4 of the micropart by the gripper or when the micro-object is outside the field-of-view of the imaging system (case 3 of Table II). Occlusions are responsible of about 17 % of failures (case 5 of Table II). The second lesson that can be retrieved is the accuracy of the visual control: the mean and standard deviations of error are summarized in Table III. There are a couple overshoots, and they do not lead to failures.

The success rate obtained is about 72 %. Error of control is the cause for around 22 % of failures (case 4 of Table II). The third conclusion to be drawn from the previous results is the importance of physical phenomena such as electrostatic and capillary forces. The presence of electric charges on both parts and fingers causes the former to move to the latter during the gripper closing and leads to the failure of the cycle. The electrostatic force is responsible for about 37 % (case 6 of Table II) of failures. Hydrometries are high enough in the scene to prevent the unsticking of the micropart on the gripper fingers because of capillary force. This phenomenon is responsible for about 24 % of failures (see case 7 of Table II of failure due to electrostatic force).

TABLE III
SUMMARIZATION OF THE RESULTS.

task	mean error	standard deviation
aligning (θ)	0.37 °	0.31 °
centering (x, y)	1.87 μm	1.61 μm
closing (e_1)	1.36 μm	0.34 μm

E. Microassembly results

Two types of 3-D devices were assembled. Each type of these devices is performed ten times. In the first hand, the assembly process targets the insertion in each other of two micro-objects (the same as those used in the micromanipulation tasks validation). More precisely, these microcomponents are assembled by their respective notches (100 μm × 100 μm × 100 μm). The mechanical play (insertion tolerance) is estimated to 3 μm. The low level of positioning and orientation errors (translation error is about 1.4 μm and orientation is about 0.5 °) enabled the insertion despite the mechanical play of 3 μm. Therefore, the 3-D microstructures built are solid without requiring external fixing process (see, Fig. 12).

It is also possible to assemble 3-D microstructures much more complex. For instance, it can be possible to assemble five micro-objects and to build a solid 3-D MEMS on 3-levels as illustrated in figure 13 (this image is acquired with the second imaging system which equipped the microassembly workcell). Even without external fixing the structure assembled is solid. Concerning the mean cycle time necessary to assemble two microparts (including positioning of the micropart one, positioning of the micropart two and the insertion of the micropart one into the micropart two) is about 40.8 seconds. Such precise assembly at real time has never been presented in the literature. With these performances, it also possible to envisage such concepts for industrial use.

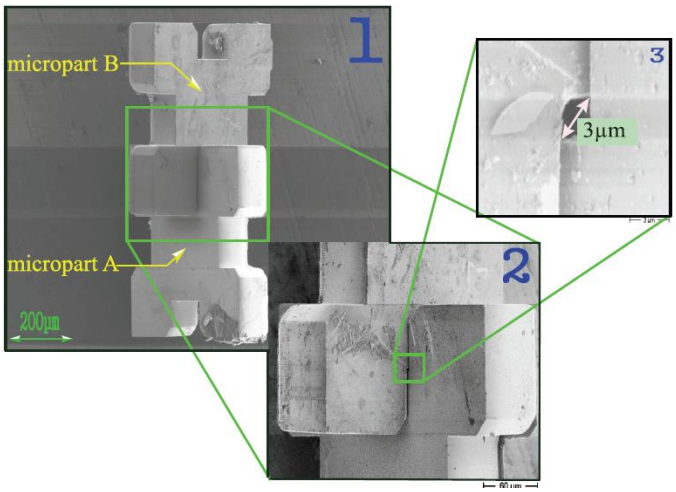

Fig. 12. Some SEM views of the 3-D structure after assembly. We can see the size of the mechanical play (insertion tolerance of the assembly) in the zoomed image (3).

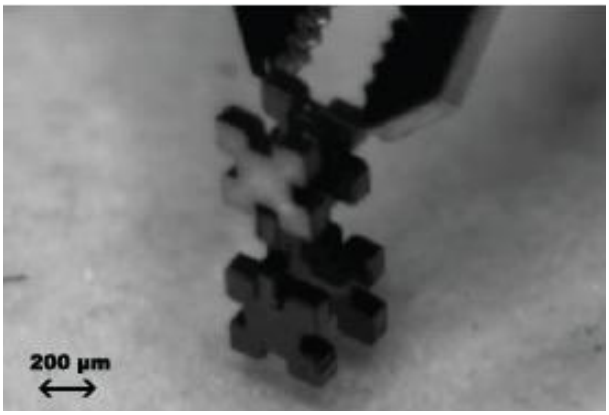

Fig. 13. Zooming picture of the complex 3-D structure assembled.

VII. Conclusion

The problems of robotic micromanipulation and microassembly of micrometric devices were studied through this paper. Despite the wealth and importance of scientific contributions in this field, there are still many efforts to get the famous flexible, modular, versatile, repeatable and precise process. In this paper, we are more interested in performing high precise micromanipulation and microassembly processes using vision feedback controls. The vision system delivers images from which a lot of information can be extracted. The problem is that high resolution (local view) and low resolution (global view) information must be caught at the same time. An interesting solution to this problem is the multiple scale imaging using a photon video microscope equipped with a tunable zoom. This multiple scale model of the video microscope is used in the visual control law.

The analysis of a complex micromanipulation or microassembly tasks leads to its decomposition into a set of basic tasks like orientation, positioning, centering, gripping, transfer, insertion, release of the micro-object. The concepts developed in this paper are validated by full-automatic pick-and-place cycles and by the assembly of 400 μm $\times$ 400 μm $\times$ 100 μm silicon micro-objects. These processes are realized using a five dof workcell which integrates a robotic system including a xyθ and a ϕz sub-systems, a two-finger gripper, a photon video microscope with controllable zoom (magnification from 0.71$\times$ to 11.5$\times$) and focus. The results of experiments demonstrate the relevance of the proposed concepts. For example, the tasks were performed with the following accuracy: the positioning error reaches 1.4 μm (for x, y and z stages) and 0.5 $^\circ$ for the orientation θ and ϕ stages.

Further work will concern the efficiency improvement of the previously proposed concepts by increasing the complexity of the operations in order to built MEMS more compact. It would also be interesting to reduce the size of these micro-objects to few micrometers and to detect the limitation of the use of the vision control feedback in the MEMS microassembly domain.

References

[1] M. Savia and H. N. Koivo, "Contact micromanipulation: Survey of strategies," *IEEE/ASME Trans. on Mechatronics*, vol. 14, pp. 504–514, 2009.

[2] N. Dechev, L. Ren, W. Liu, W. Cleghorn, and J. Mills, "Development of a 6 degree of freedom robotic micromanipulation for use in 3d mems microassembly," in *IEEE ICRA*, Orlando, Fl., May 2006.

[3] Kim, J.; Seo, T. W.; Kang, D. S.; Kim, H. S. "Dual servo control of a high-tilt 3-dof microparallel positioning platform," *IEEE/ASME Trans. on Mechatronics*, vol. 14 (5), pp. 616–625, 2009.

[4] U. Srinivasan, D. Liepmann, and R. T. Howe, "Microstructure to substrate self-assembly using capillary forces," *J. of Microelectronmechanical Systems*, vol. 10, no. 1, pp. 17–24, 2001.

[5] J. A. Gaines, G. Yang and B J. Nelson, "A surpervisory wafer-level 3d microassembly system for hybrid mems fabrication," *J. of Intelligent and Robotic Systems*, vol. 37, pp. 43–68, 2003.

[6] J. T. Feddema and T. R. Christenson, "Parallel assembly of high aspect ration microstructures," in *Part of SPIE Conf. on Microrobotics and Microassembly*, USA, 1999, vol. 3834, pp. 153–164.

[7] B. Tamadazte, T. Arnould, S. Dembélé, N. Le Fort-Piat, and E. Marchand, "Real-time vision-based microassembly of 3d mems," in *IEEE/ASME Int. Conf. on Advanced Intelligent Mechatronics, AIM 2009*, Singapore, July 2009, pp. 94–99.

[8] R. Devanathan, S. Wenting, S. Chai, and A. Shacklock, "Multi view and multi scale image based visual servo for micromanipulation," *Studies in Computational Intelligence*, vol. 8, pp. 105–133, 2006.

[9] S. Fatikow, T. Wich, H. Hulsen, T. Sievers, and M. Jahnisch, "Microrobot system for automatic nanohandling inside a scanning electron microscope," *IEEE/ASME Trans. on Mechatronics*, vol. 12, pp. 244–252, june, 2007.

[10] S. Ralis, B. Vikramaditya, and B. J. Nelson, "Micropositioning of a weakly calibrated microassembly system using coarse-to-fine visual servoing strategies," *IEEE Trans. on Electronics Packaging Manufacturing*, vol. 23 (2), pp. 123–131, 2000.

[11] A. Ferreira, C. Cassier, and S. Hirai, "Automatic microassembly system assisted by vision servoing and virtual reality," *IEEE/ASME Trans. on Mechatronics*, vol. 9 (2), p. 321333, june, 2004.

[12] W. Sun and T. Chin, "Image-based visual servo for micromanipulation : a multiple-view and multiple-scale approach," in *Int. Symposium on Micro-Nanomechatronics and Human Science*, 2004, pp. 341–346.

[13] X. Tao, H. Cho, and Y. Cho, "Microassembly of peg and hole using active zooming," in *Proc. of SPIE, the Int. Society for Optical Engineering*, Japon, 2005, pp. 1–12.

[14] R. S. Fearing, "Survey of sticking effects for micro parts handling," in *IEEE IROS*, Pittsburgh, PA, 1995, pp. 212–217.

[15] B. Espiau, F. Chaumette, and P. Rives, "A new approach to visual servoing in robotics," *IEEE Trans. Robotics and Automation*, vol. 8, no. 3, pp. 313–326, Jun. 1992.

[16] S. Hutchinson, G. Hager, and P. Corke, "A tutorial on visual servo control," *IEEE Trans. Robotics and Automation* vol. 12, no. 5, pp. 651–670, Oct. 1996.

[17] Y. Zhou and B. J. Nelson, "Calibration of a parametric model of an optical microscope," *Optical Engeenering*, vol. 38, no. 12, pp. 1989–1995, 1999.

[18] M. Ammi, V. Fremont, and A. Ferreira, "Flexible microscope calibration using virtual pattern for 3-d telemicromanipulation," *IEEE ICRA*, Spain, 2005, pp. 3888–3893.
[19] R. Y. Tsai, "A versatile camera calibration technique for high-accuracy 3d machine vision metrology using off-the-shelf tv cameras and lenses," *IEEE J. of Robotics and Automation*, vol. RA-3, no. 4, pp. 323–344, 1987.
[20] B. Tiggs, "Autocalibration from planar scenes," *In Porc. 5th European Conf. on Computer Vision*, vol. 1406, 1998, pp. 89.
[21] X. Liu, W. Wong and Y. Sun, "Robust contact detection in micormanipulation using computer vision microscopy," *In Porc. IEEE Engineering Medical Biol. Society*, pp. 2219–2222, 2006.
[22] E. Malis, "Improving vision-based control using efficient second-order minimization techniques," in *IEEE ICRA*, New-Orleans, USA, May, 2004, pp. 1843–1848.
[23] G. Silveira and E. Malis, "Real time tracking under arbitrary illumination changes," *In Computer Vision and Pattern Recognition*, pp. 1–6, 2007.
[24] S. Benhimane and E. Malis, "Homography-based 2d visual tracking and servoing," *The Int. J. of Robotics Research (IJRR)*, vol. 26, no. 7, pp. 661–676, 2007.
[25] Y. Sun, S. Duthaler, and B. J. Nelson, "Autofocusing algorith selection in computer microscopy," in *Proceedings of IEEE/RSJ IROS*, Canada, 2005, pp. 70–76.
[26] P. N. J. Agnus and N. Chaillet, "Overview of microgrippers and design of a micromanipulation station based on mmoc microgripper," *In Proc. of IEEE CIRA*, Finland, 2005, pp. 117–123.

Brahim Tamadazte holds a Ph.D. in Automation and Computer Science from the "Université de Franche-Comté" in 2009 and a MS degree in Robotics and Intelligent Systems from the " Université Pierre et Marie Curie (Paris VI)" in 2005, in France. Before, Brahim has also trained as an engineer in Automation Systems at the "Université Mouloud Mammeri de Tizi-Ouzou" from Algeria. During his Ph.D thesis, Brahim has developed some vision algorithms and vision-based control laws (image-based visual servoing and pose visual servoing) for the automation of MEMS (Micro-Electro-Mechanical-Systems) and MOEMS (Micro-Optico-Electro-Mechanical-Systems) handling and assembly. He also has an interest to the development of new calibration methods dedicated to modeling imaging systems equipped with high magnification lens as the optical microscopes. Actually, Brahim is an associate professor at the ENSMM (National Engineering School of Mechanics and Microtechniques) and makes his research works at the AS2M (Automatic Control and Micro-Mechatronic Systems) department of FEMTO-ST Institute.

Nadine Le-Fort Piat Nadine Le Fort-Piat received her Ph.D. in Systems in Automation and Signal Processing at the University of Technology in Compiègne (UTC) in 1984. She became associate professor at UTC Compiègne in 1984 and professor at the ENSMM (National Engineering School of Mechanics and Microtechniques - Besançon) in 1998. She is a member of the AS2M department of the Institute FEMTO-ST, UMR CNRS 6174, in Besançon. Her research areas concern perception and advanced control strategies based on visual servoing and reinforcement learning for automation of distributed microrobotic systems.

Sounkalo Dembélé received his Ph.D. in Systems Control at University of Franche Comté Besançon in 1993. He became Electronics Engineer at ENSMM (National Engineering School of Mechanics and Microtechniques) Besançon in 1994 where he developed a mobile robot, Associate Professor at University of Franche Comté Besançon in 1995. His is a member of FEMTO-ST Institute where he works on robotic assembly of MEMS and MOEMS. After swarm robotics, control of an ultrasonic linear micromotor and fringe based tracking, his researches currently involve Novel View Synthesis by mosaicing and trifocal transfer, shape-from-focus based tracking, feature based tracking, calibration of microscope, vision based control.